Impact of Impeller Structural Parameters on Cavitation of High-speed Aviation Piston Pump

Hua Fang, Hanyu Gao, Bo Yang, Yijie Lu, Hao Liu*, and Xiaoping Ouyang*

State Key Laboratory of Fluid Power & Mechatronic Systems, Zhejiang University, Hangzhou, China
E-mail: Hua Fang. fhua@zju.edu.cn, Hanyu Gao. henrygao@zju.edu.cn, Bo Yang. yang_bo@zju.edu.cn, Yijie Lu. luyijie@zju.edu.cn, Hao Liu*. haoliu7850052@zju.edu.cn, Xiaoping Ouyang*, ouyangxp@zju.edu.cn
* State Key Laboratory of Fluid Power & Mechatronic Systems, Zhejiang University, Hangzhou, China

Abstract

Impellers can effectively suppress cavitation in high-speed aviation piston pumps. However, the effects of different impeller structural parameters on cavitation are still unclear. In this paper, a CFD model of a high-speed aviation piston pump with an integrated impeller is established, and the effects of various structural parameters on cavitation are analyzed in detail based on the orthogonal test method. Simulation results show that the blade outlet width has the greatest effect on cavitation, followed by the blade outlet angle, while the impeller inlet diameter has the least effect. Within a certain range, increasing the impeller inlet diameter and blade outlet angle can effectively suppress cavitation, but the cavitation suppression effect will decrease after exceeding critical thresholds. Increasing the blade outlet width can suppress pump cavitation. The effects of different impeller structural parameters on cavitation under different outlet pressures and speeds are further analyzed. Simulation results show that the speed has a greater impact on cavitation than the outlet pressure. The results of this paper can be used to guide the design and optimization of impellers for high-speed aviation piston pumps.

Keywords: Aviation piston pump, impeller, cavitation, suction port, CFD model

1 Introduction

With many advantages such as high-power density, high output pressure, high efficiency, and variable control, axial piston pumps are a type of volumetric hydraulic pump widely used in aircraft hydraulic systems (also known as aviation piston pumps (APPs)). The development trend of efficient and lightweight aircraft has prompted the development of aviation hydraulic systems and their key components, APPs, towards higher power density. For APPs in electrical motor-driven pumps, increasing the speed is one of the effective ways to increase power density [1]. However, as the speed of the APP increases, the flow rate in the oil suction passage increases, causing the pressure in these regions to drop sharply below the air separation pressure or saturated vapor pressure, resulting in the precipitation of gas dissolved in the oil, and even the gasification of the oil itself, i.e., cavitation. When bubbles enter the high-pressure regions with the oil, they will shrink or collapse rapidly, causing cavitation damage such as erosion or detachment on the surface of components, thereby reducing the reliability and service life of APPs [2].

At present, there are two main solutions to suppress cavitation in high-speed APPs. The first is to optimize the suction passage structure. The main principle is to reduce the pressure loss in the suction passage by optimizing the suction passage structure between the suction port and the piston chamber[3-6]. The second is to increase the suction pressure. By increasing the pressure at the suction port, the pressure loss in the suction channel can be compensated. Studies have shown that the effect of optimizing the suction passage structure on suppressing cavitation is very limited [7], and increasing the suction pressure is a more effective solution. There are three main methods to increase the suction pressure, namely, pressurizing the tank [8], adding a booster pump to the suction pipeline, and adding an impeller in the suction port of APP[9]. Among them, the constraints on the size and weight of the aircraft hydraulic system limit the diameter of the suction pipeline, and it is difficult to compensate for the pressure loss between the tank and the suction port by increasing the tank pressure. Meanwhile, adding a booster pump to the suction pipeline will reduce the reliability of the aircraft hydraulic system. In contrast, integrating an impeller in the suction port allows the APP to operate normally, even under very low suction pressure conditions[10]. Therefore, compared with the other two methods, adding an impeller in the suction port is a better method.

At present, the research on impellers mainly focuses on the relationship between structural parameters (such as blade outlet width [11], impeller inlet diameter [12-13], blade outlet angle [14-16]) and impeller performance, and various methods are used to optimize the impeller structural parameters to obtain the optimal solution of boost pressure, efficiency, and energy loss [17-23]. However, there are few studies on impellers in APPs. Chen et al. [24] studied the energy loss and distribution of the impeller based on the entropy generation theory. Dong et al. [25] verified the cavitation suppression effect of the impeller in the speed range of 1000 rpm-5000 rpm through simulation and experiments. However, the research on the influence of impeller structural parameters on cavitation in high-speed APPs is still limited.

In this paper, a CFD model of a high-speed APP with an integrated impeller is established, and the effect of impeller structural parameters, such as impeller inlet diameter, blade outlet width, and blade outlet angle, on cavitation, is analyzed based on the orthogonal test method, and reveals the effects of impeller structural parameters on cavitation under different pressure and speed conditions. The results of this paper can be used for the design and optimization of impellers in high-speed APPs.

The rest of the paper is organized as follows. In Section 2, a CFD model of a high-speed APP with an integrated impeller is established, and the optimal impeller structural parameter combination is obtained based on the orthogonal test method. In Section 3, the effects of different impeller structural parameters on cavitation are analyzed in detail, and the effect of structural parameter changes on cavitation under different operating conditions is analyzed. The conclusions are provided in Section 4.

2 Modeling

2.1 APP and impeller

The structure of the APP studied in this paper is shown in Figure 1. The piston is located in the cylinder chamber of the cylinder block and is connected to the swash plate through a slider hinged on the spherical heads. Driven by the coordinated motion of the shaft and the swash plate, the piston can both rotate around the axis and reciprocate in a straight line. The reciprocating motion of the piston causes volume in the cylinder chamber to change, thereby completing the suction and discharge stroke of the piston pump.

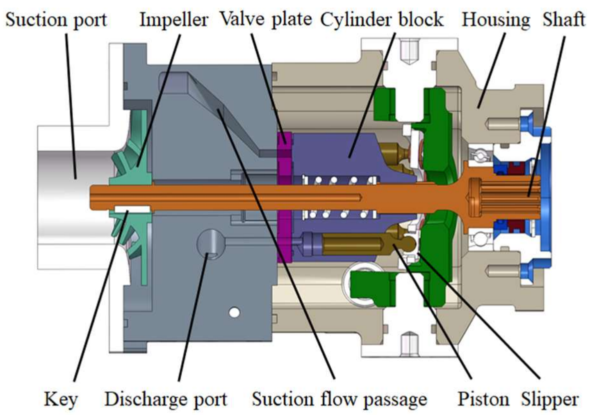

Figure 1: Structure of APP integrated with impeller.

Compared to traditional APPs, the high-speed APP studied in this paper integrates an impeller in the suction port. The impeller structure is shown in Figure 2. The impeller is rigidly connected to the APP through a flat key and rotates synchronously with the APP shaft. The main structural parameters of the impeller include the hub diameter d_h, the impeller inlet diameter D_j, the blade inlet diameter D_1, the impeller outlet diameter D_2, the blade inlet width b_1, the blade outlet width b_2, the blade inlet angle β_1, the blade outlet angle β_2, and the blade wrap angle φ. Under the action of centrifugal force, the oil in the impeller is transported to the suction flow passage of the APP. Simultaneously, the oil in the suction port is continuously replenished into the impeller under the action of the pressure difference.

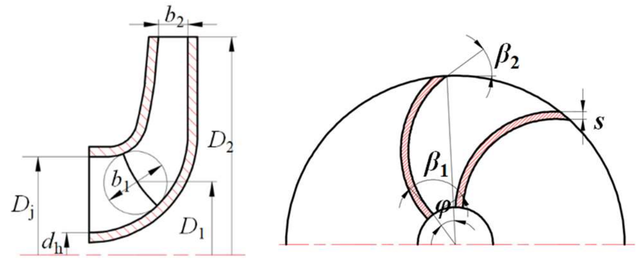

Figure 2: Impeller structure.

Table 1: Parameters of APP and impeller

Parameters	Values	Units
Displacement	2	mL/r
Number of pistons	9	null
Inclination of the swash plate	17	°
Impeller outlet diameter	49	mm
Hub diameter	11	mm
Blade inlet angle	15	°
Blade wrap angle	150	°

2.2 CFD modeling

The numerical model used in this paper integrates a turbulence model[26]and the full cavitation model proposed by Singhal et al.[27], and considers three liquid properties, namely cavitation, aeration and liquid compressibility, which have been successfully applied to CFD models of APPs [28]. The transport equation for cavitation vapor can be described as

$$\frac{\partial}{\partial_t}\int_{\Omega(t)}\rho f_{\mathrm{V}}\mathrm{d}\Omega+\int_{\sigma}\rho\left((\vec{v}-\vec{v_{\sigma}})\cdot\vec{n}\right)f_{\mathrm{V}}\mathrm{d}\sigma= \int_{\sigma}\rho\left(D_{\mathrm{V}}+\frac{\mu_{\mathrm{t}}}{\sigma_{\mathrm{f}}}\right)\cdot(\nabla f_{\mathrm{V}}\cdot\vec{n})\mathrm{d}\sigma+\int_{\Omega}(R_{\mathrm{e}}-R_{\mathrm{c}})\mathrm{d}\Omega \tag{1}$$

$$R_{\mathrm{e}}=C_{\mathrm{e}}\cdot\rho_{\mathrm{l}}\rho_{\mathrm{V}}\left[\frac{2}{3}\frac{p-p_{\mathrm{V}}}{\rho_{\mathrm{l}}}\right]^{1/2}\left(1-f_{\mathrm{V}}-f_{\mathrm{g}}\right) \tag{2}$$

$$R_{\mathrm{c}}=C_{\mathrm{c}}\cdot\rho_{\mathrm{l}}\rho_{\mathrm{V}}\left[\frac{2}{3}\frac{p-p_{\mathrm{V}}}{\rho_{\mathrm{l}}}\right]^{1/2}f_{\mathrm{V}} \tag{3}$$

where $\Omega(t)$ is the control volume as a function of time, σ is the surface area of the control volume, $\vec{n}$ is the surface normal of σ, ρ is the density of the hydraulic oil, $\vec{v}$ is the fluid velocity, $\vec{v_\sigma}$ is the surface motion velocity, μ_t is the turbulent dynamic viscosity, p is the static pressure, f_v is the mass fraction of vapor, D_v is the diffusivity of vapor, σ_f is the turbulent Schmidt number, R_e is the vapor generation rate, R_c is the vapor condensation rate, p_V is the liquid vapor pressure, ρ_l is the liquid density and ρ_V is the vapor density. Among them, c_e=0.02 and c_c=0.01 are the coefficients of R_e and R_c, respectively.

The full cavitation model takes into account the mass fraction of non-condensable gas in the liquid f_g, which can be calculated as

$$\frac{\partial}{\partial_t}\int_{\Omega(t)}\rho f_d d\Omega + \int_\sigma \rho\left((\vec{v}-\vec{v_\sigma})\cdot\vec{n}\right)f_d d\sigma = \int_\sigma \rho\left(D_d + \frac{\mu_t}{\sigma_f}\right)\cdot(\nabla f_d\cdot\vec{n})d\sigma + \int_\Omega \frac{\rho(f_d - f_{de})}{\tau}d\Omega \tag{4}$$

$$f_{de} = \frac{p}{p_{der}}\cdot f_{der} \tag{5}$$

$$f_g + f_d = constant \tag{6}$$

where f_d is the mass fraction of dissolved gas, f_{de} is the equilibrium mass fraction of non-condensable gas at the local pressure, D_d is the diffusivity of dissolved gas, τ is the gas absorption/release time, and p_{der} is the reference pressure of the equilibrium mass fraction of dissolved gas.

In the full cavitation model, the hydraulic fluid is considered as a fluid mixture including liquid, vapor, and free gas, and the density of the mixture can be calculated as:

$$\frac{1}{\rho} = \frac{f_V}{\rho_V} + \frac{f_g}{\rho_g} + \frac{1 - f_V - f_g}{\rho_l} \tag{7}$$

The compressibility of oil is described by the bulk modulus. The relationship between the bulk modulus K and liquid density ρ_l is

$$K = \frac{\rho_{lr}}{\frac{\partial \rho_l}{\partial p}} \tag{8}$$

where ρ_{lr} is the liquid density at the reference pressure. Since the vapor density is assumed to be constant in this paper, the density of the non-condensable gas is calculated as

$$\rho_g = \frac{Wp}{RT} \tag{9}$$

where W is the molecular weight of gas, R is the universal gas constant, and T is the thermodynamic temperature.

The non-condensable gas volume fraction α_g and vapor volume fraction α_V can be calculated as:

$$\alpha_g = f_g\frac{\rho}{\rho_g} \tag{10}$$

$$\alpha_V = f_V\frac{\rho}{\rho_V} \tag{11}$$

The above numerical model is implemented in the commercial CFD software Pumplinx. Unlike traditional centrifugal pumps, the impeller integrated in the APP pressurizes the oil and transports it through the suction passage to the piston chamber with a constantly changing volume. Since it is difficult to accurately simulate the above process using the impeller model alone, the model established in this paper integrates the impeller and APP. Moreover, since this paper mainly studies the cavitation phenomenon in APPs, the established CFD model does not consider the lubrication interface and the leakage between friction pairs. As shown in Figure 3, the fluid domain of the APP with an impeller can be divided into six regions, namely the suction passage, the impeller region, the discharge passage, the valve plate suction chamber, the valve plate discharge chamber, and the piston chamber. To accurately simulate the operating conditions of the APP, this paper used the transient simulation method for numerical simulation.

In the established CFD model, the suction port and discharge port of APP are set as pressure inlet and pressure outlet respectively, the piston chamber is set as the rotation boundary condition, the valve plate suction chamber and valve plate discharge chamber are set to be stationary, the wall boundary is defined as a no-slip boundary, and the contact surface of the adjacent area is set as an interface to ensure the continuity of the oil flow. Since the impeller rotates synchronously with the piston chamber, the impeller is set to rotate relative to each other, and the adjacent surface of the impeller and the suction passage is set as an interface. The boundary conditions of the established model are detailed in Table 2.

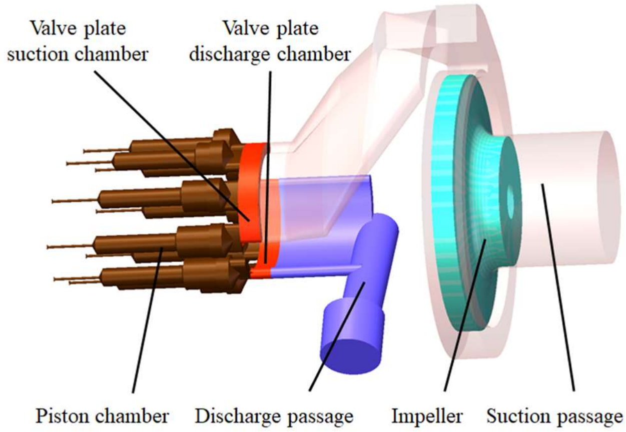

Figure 3: Fluid domain of APP with impeller.

Table 2: Boundary conditions of the CFD model.

Parameters	Values	Units
Density	837	kg/m^3
Dynamic viscosity	0.01155	Pa·s
Saturated vapor pressure	400	Pa
Inlet pressure	0.2	MPa
Outlet pressure	28	MPa
Speed	12000	rpm
displacement of the pump	2	mL/r

2.3 Orthogonal test design

Orthogonal test design is an effective method for studying multiple factors and levers, which can obtain statistically equivalent results to full factorial experiments with a limited number of experiments[17]. In this paper, two parameters are selected as evaluation indicators for measuring impeller effect, one is the impeller inlet and outlet pressure difference Δp, and the other is the average gas volume fraction in the piston chamber during one rotation of the APP per_g. The orthogonal tests are designed to investigate three structural parameters of the impeller: the impeller inlet diameter D_j, the blade outlet width b_2, and the blade outlet angle β_2, and the L9（3^3）orthogonal test results are shown in Table 3. Keeping the other structural parameters of the impeller constant, numerical simulation is performed according to the parameter combination in Table 3. The quantitative changes of Δp and per_g are utilized to evaluate the effects of different parameter combinations on cavitation.

Table 3: Orthogonal test results.

No.	Structural parameters			Δp (MPa)	per_g
	D_j (mm)	b_2 (mm)	β_2 (°)		
1	21	2	20	0.244038	1.1946%
2	21	2.5	40	0.283537	1.0507%
3	21	3	30	0.310530	0.9723%
4	25	2	40	0.257847	1.1411%
5	25	2.5	30	0.286801	1.0390%
6	25	3	20	0.302210	0.9927%
7	27	2	30	0.259146	1.1329%
8	27	2.5	20	0.270655	1.0920%
9	27	3	40	0.299906	0.9995%

The range analysis results of Δp and per_g are shown in Table 4. In Table 4, k_i (i=1,2,3) represents the average result of three structural parameters D_j, b_2, and β_2 at the i-th value, reflecting the average impact of different structural parameters on the results at a certain value. For example, k_1, k_2, and k_3 in the first row to the third row of the first column in Table 4 represent the average Δp of three impellers when D_j= 21mm, 25mm, and 27mm, respectively. The meanings of other parameters in Table 4 are similar. R is the difference between the maximum and minimum values of each structural parameter, reflecting the impact of changes in a single structural parameter on the results.

From Table 4, it can be found that, for both Δp and per_g, the range of b_2 is significantly higher than those of the other two structural parameters. Therefore, it can be concluded that within the range of structural parameters in Table 3, b_2 has the greatest effect on Δp and per_g, followed by β_2, while D_j has the least effect. The optimal combination of three structural parameters determined by the range analysis is D_j=25mm, b_2=3mm, and β_2=30°.

Table 4: Range analysis results.

		D_j	b_2	β_2
Δp	k_1	0.279368	0.253677	0.272301
	k_2	0.282286	0.280331	0.285492
	k_3	0.276569	0.304215	0.280430
	R	0.005717	0.050538	0.013191
per_g	k_1	1.072522	1.156170	1.093081
	k_2	1.057581	1.060560	1.048041
	k_3	1.074780	0.988154	1.063763
	R	0.017199	0.168017	0.04504

To further explore the effects of different structural parameters on cavitation, the effect of a single structural parameter on Δp and per_g is analyzed by keeping any two structural parameters unchanged, based on the structural parameter combination where D_j=25mm, b_2=3mm, and β_2=30°.

3 Results and discussions

3.1 Analysis of the effect of structural parameters

First, under the condition of 12000 rpm (speed)and 28MPa (outlet pressure), b_2=3mm and β_2=30° are kept unchanged, and D_j is set to 21 mm, 23 mm, 25 mm, 27 mm, and 29 mm, respectively. The obtained Δp and per_g are shown in Figure 4. It can be observed that with the increase of D_j, the boosting effect first increases and then weakens. When D_j exceeds 25 mm, the boosting effect begins to weaken. The reason is that the increase of D_j increases the cross-sectional area of the impeller flow passage and reduces the inlet flow velocity, thereby reducing flow friction loss and impact loss, and improving boosting efficiency. However, as D_j further increases, the flow velocity continues to decrease, the kinetic energy of the oil entering the impeller is insufficient, causing problems such as flow separation and vortex, which reduces the boosting effect. In contrast to the trend of Δp, the per_g value first decreases and then increases with the increase of D_j. When D_j exceeds 25 mm, per_g begins to increase. The results show that there exists an optimal value of D_j to optimize the boosting effect and cavitation suppression effect of the impeller.

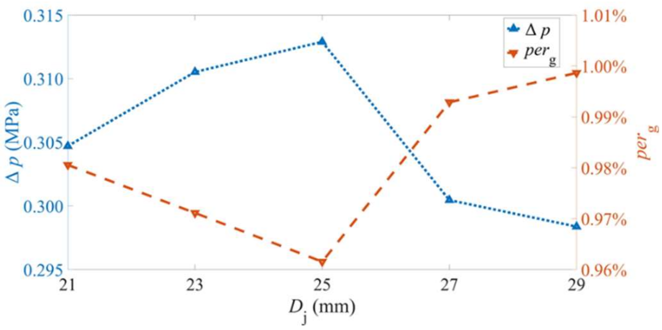

Figure 4: Effects of D_j on Δp and per_g.

Then, keeping D_j=25mm and β_2=30° unchanged, and setting b_2 to 1.5mm, 2mm, 2.5mm, 3mm, and 3.5mm, respectively. The obtained Δp and per_g are shown in Figure 5. It can be seen that with the increase of b_2, the boosting effect of the impeller gradually improves. The reason is that the increase of b_2 increases the cross-sectional area of the impeller and reduces the impeller outlet velocity, thereby reducing friction loss and turbulence loss, and improving the boosting effect. On the contrary, per_g gradually decreases with the increase of b_2. The simulation results indicate that a larger b_2 can be selected when designing the impeller. However, increasing b_2 will increase the radial size of the impeller and increase the weight of the APP. Therefore, the selection of b_2 needs to strike a balance between weight and boosting effect.

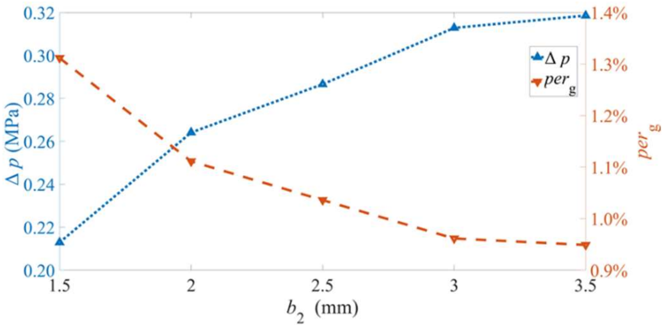

Figure 5: Effects of b_2 on Δp and per_g.

At last, keeping D_j=25mm and b_2=3mm unchanged, settingβ_2 to 10°, 20°, 30°, 40° and 45°, respectively. The obtained Δp and per_g are shown in Figure 6. It can be seen that with the increase of β_2, the boosting effect first increases and then weakens. When β_2 exceeds 30°, the boosting effect begins to weaken. The reason is that the increase of β_2 increases the tangential velocity at the impeller outlet and the theoretical head, that is, the boosting effect is improved. However, continuing to increase β_2 will intensify oil flow separation and vortex, intensify energy dissipation, and reduce the boosting effect. Contrary to the changing trend of Δp, per_g first decreases and then increases with the increase of β_2. When β_2 exceeds 30°, per_g begins to rise. Therefore, there exists an optimal β_2 that can achieve the optimal boosting effect and cavitation suppression effect at the same time.

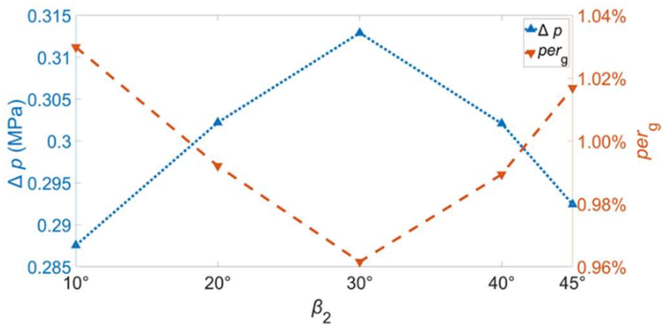

Figure 6: Effects of β_2 on Δp and per_g.

3.2 Analysis of the effect of operating conditions

To further analyze the effects of the impeller structural parameters on cavitation, simulations need to be carried out under different pressure and speed conditions.

3.2.1 Analysis of the effect of outlet pressure

The speed of APP is set to be constant at 12000 rpm, and the outlet pressures are set to 7MPa, 14MPa, 21MPa, 28MPa, and 35MPa, respectively. The obtained Δp and per_g are shown in Figures 7 and 8, respectively. It can be seen from Figure 7 that the change trend of Δp under different outlet pressures is similar, that is, with the increase of D_j, the boosting effect first increases and then weakens. The Δp of the impeller with the same D_j increases with the rise of outlet pressure. Taking the impeller with D_j=29mm, b_2=3mm, and β_2=30° as an example, as the outlet pressure increases from 7MPa to 35MPa, Δp increases from 0.295MPa to 0.299MPa. It can be seen from Figure 8 that the change trend of per_g under different outlet pressures is also similar, that is, with the increase of D_j, per_g first decreases and then increases. The per_g of the impeller with the same D_j decreases with the rise of outlet pressure. Taking the impeller with D_j=29mm, b_2=3mm, and β_2=30° as an example, as the outlet pressure increases, the maximum value of per_g decreases from 1.153% to 0.980%.

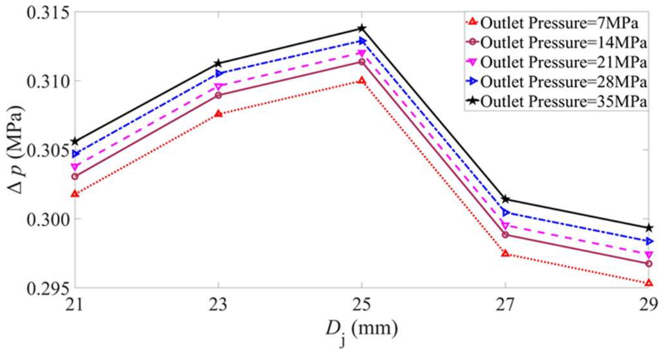

Figure 7: Effects of D_j on Δp under different outlet pressures.

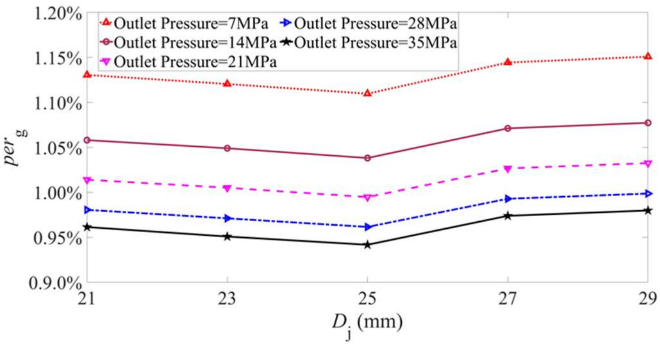

Figure 8: Effects of D_j on per_g under different outlet pressures.

The speed of APP is set to be constant at 12000 rpm, and the outlet pressures are set to 7MPa, 14MPa, 21MPa, 28MPa, and 35MPa, respectively. The obtained Δp and per_g are shown in Figures 9 and 10, respectively. It can be seen from Figure 9 that when the outlet pressure is constant, Δp is positively correlated with b_2. The Δp of the impeller with the same b_2

continues to increase with the rise of outlet pressure. Taking the impeller with D_j=25mm, b_2=1.5mm, and β_2=30° as an example, Δp increases from 0.209MPa to 0.214MPa as the outlet pressure rises from 7MPa to 35MPa. It can be seen from Figure 10 that when the outlet pressure is constant, per_g is negatively correlated with b_2. The per_g of the impeller with the same b_2 continues to decrease with the rise of outlet pressure. Taking the impeller with D_j=25mm, b_2=1.5mm, and β_2=30° as an example, the maximum value of per_g decreases from 1.48% to 1.29% as the outlet pressure rises from 7MPa to 35MPa.

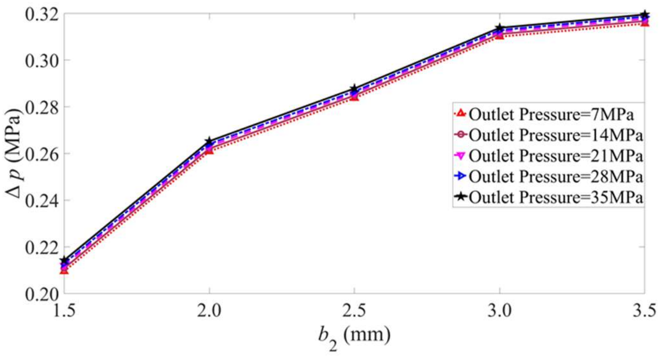

Figure 9: Effects of b_2 on Δp under different outlet pressures.

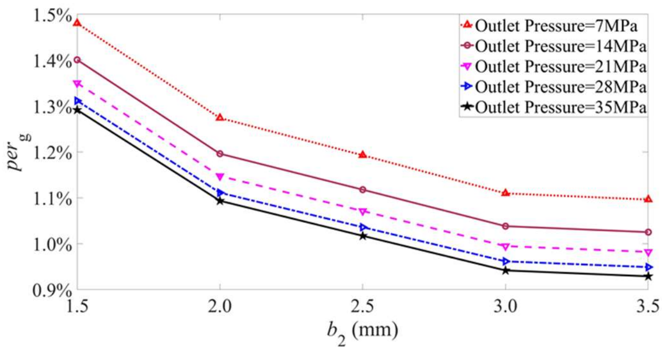

Figure 10: Effects of b_2 on per_g under different outlet pressures.

The speed of APP is set to be constant at 12000 rpm, and the outlet pressures are set to 7MPa, 14MPa, 21MPa, 28MPa, and 35MPa, respectively. The obtained Δp and per_g are shown in Figures 11 and 12, respectively. It can be seen from Figure 11 that the change trend of Δp under different outlet pressures is similar, that is, with the increase of β_2, the boosting effect first increases and then weakens. The Δp of the impeller with the same β_2 increases slightly with the rise of outlet pressure. Taking the impeller with D_j=25mm, b_2=3mm, and β_2=10° as an example, as the outlet pressure increases from 7MPa to 35MPa, Δp rises from 0.285MPa to 0.289MPa. It can be seen from Figure 12 that the change trend of per_g under different outlet pressures is also similar, that is, with the increase of β_2, per_g first decreases and then increases. The per_g of the impeller with the same β_2 decreases with the rise of outlet pressure. Taking the impeller with D_j=25mm, b_2=3mm, and β_2=10° as an example, as the outlet pressure increases, the maximum value of per_g decreases from 1.18% to 1.01%.

In summary, it can be found that with the increase of outlet pressure, the boosting effect and cavitation suppression effect are slightly improved. The reason is that with the increase of APP outlet pressure, the oil compression volume increases, resulting in a decrease in output flow, causing the impeller operating point to shift slightly to the left along the P-Q curve, that is, the boosting effect is slightly enhanced, thereby improving the cavitation suppression effect.

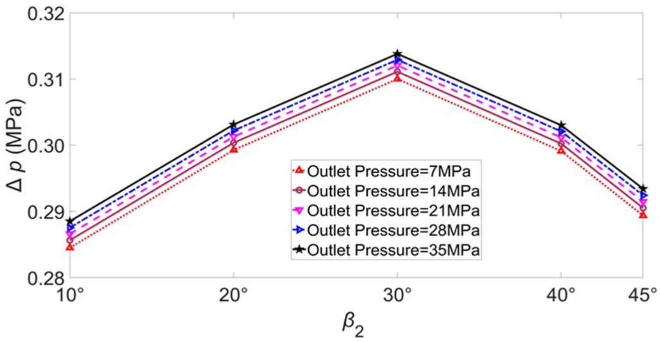

Figure 11: Effects of β_2 on Δp under different outlet pressures.

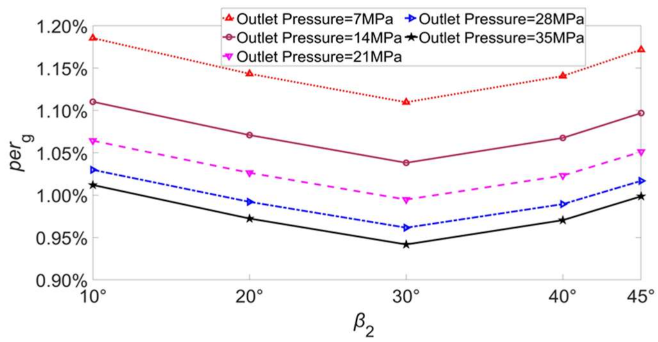

Figure 12: The effect of β_2 on per_g under different outlet pressures.

3.2.2 Analysis of the effect of speed

The outlet pressure of APP is set to be constant at 28MPa, and the speeds are set to 6000rpm, 8000rpm, 10000rpm, and 12000rpm, respectively. The obtained Δp and per_g are shown in Figures 13 and 14, respectively. It can be seen from Figure 13 that the change trend of Δp under different speeds is similar, that is, with the increase of D_j, the boosting effect first increases and then weakens. The Δp of the impeller with the same D_j increases sharply with the rise of speed. Taking the impeller with D_j=29mm, b_2=3mm, and β_2=30° as an example, with the speed increasing from 6000 rpm to 12000 rpm, Δp rises from 0.075 MPa to 0.298 MPa. It can be seen from Figure 14 that the change trend of per_g under different speeds is also similar, that is, with the increase of D_j, per_g first decreases and then increases. The per_g of the impeller with the same D_j decreases sharply with the rise of speed. Taking the impeller with D_j=29mm, b_2=3mm, and β_2=30° as an example, with the speed increasing from 6000 rpm to 12000 rpm, the maximum value of per_g decreases from 1.40% to 1.00%.

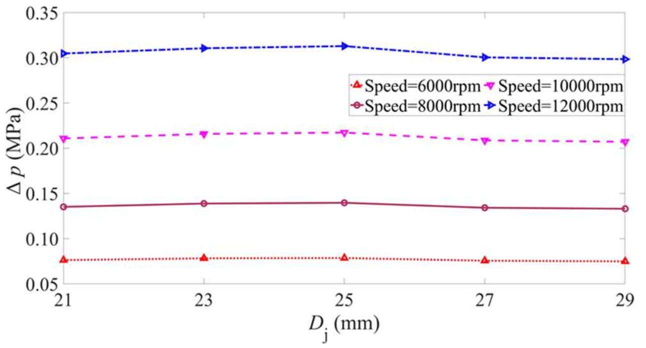

Figure 13: Effects of D_j on *Δp under different speeds.*

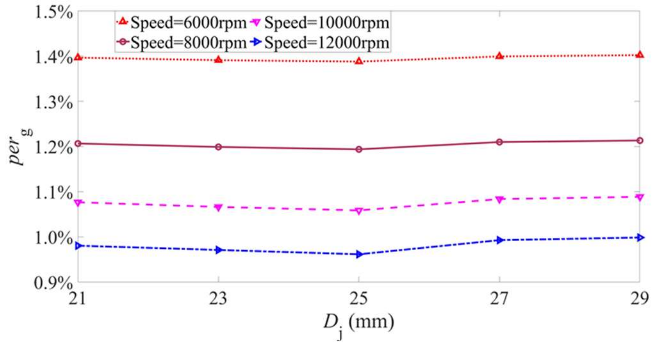

Figure 14: Effects of D_j on per_g under different speeds.

The outlet pressure of APP is set to be constant at 28MPa, and the speeds are set to 6000rpm, 8000rpm, 10000rpm, and 12000rpm, respectively. The obtained Δp and per_g are shown in Figures 15 and 16, respectively. It can be seen from Figure 15 that when the speed is constant, Δp is positively correlated with b_2. The Δp of the impeller with the same b_2 continues to increase with the rise of speed. Taking the impeller with D_j=25mm, b_2=1.5mm, and β_2=30° as an example, with the speed increases from 6000 rpm to 12000 rpm, Δp rises from 0.051 MPa to 0.213 MPa. It can be seen from Figure 16 that when the speed is constant, per_g is negatively correlated with b_2. The per_g of the impeller with the same b_2 continues to decrease with the rise of outlet pressure. Taking the impeller with D_j=25mm, b_2=1.5mm, and β_2=30° as an example, with the speed increasing from 6000 rpm to 12000 rpm, the maximum value of per_g decreases from 1.50% to 1.31%.

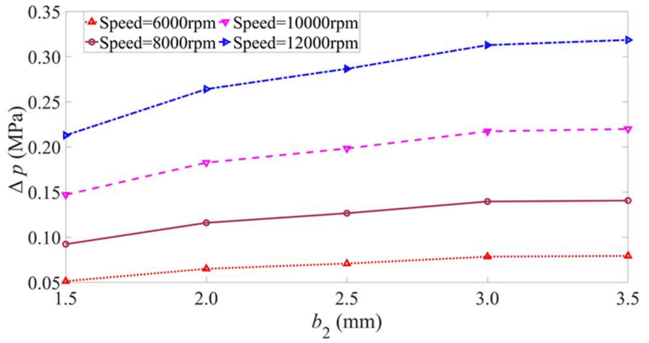

Figure 15: Effects of b_2 on Δp under different speeds.

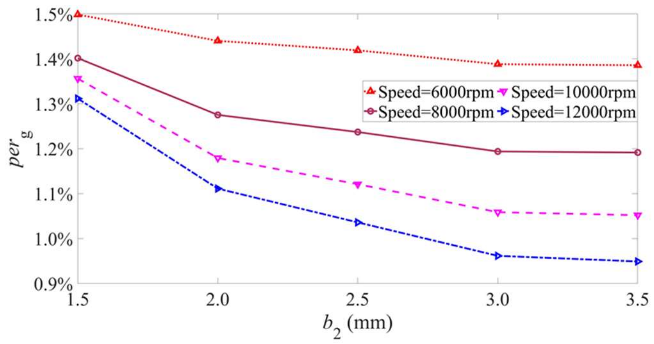

Figure 16: Effects of b_2 on per_g under different speeds.

The outlet pressure of APP is set to be constant at 28MPa, and the speeds are set to 6000rpm, 8000rpm, 10000rpm, and 12000rpm, respectively. The obtained Δp and per_g are shown in Figures 17 and 18, respectively. It can be seen from Figure 17 that the change trend of Δp under different speeds is similar, that is, with the increase of β_2, the boosting effect first increases and then weakens. The Δp of the impeller with the same β_2 increases with the rise of speed. Taking the impeller with D_j=25mm, b_2=3mm, and β_2=10° as an example, as the speed rises from 6000 rpm to 12000 rpm, Δp rises from 0.072 MPa to 0.288 MPa. It can be seen from Figure 18 that the change trend of per_g under different speeds is also similar, that is, with the increase of β_2, per_g first decreases and then increases. The per_g of the impeller with the same β_2 decreases with the rise of speed. Taking the impeller with D_j=25mm, b_2=3mm, and β_2=10° as an example, as the speed rises from 6000 rpm to 12000 rpm, the maximum value of per_g decreases from 1.41% to 1.03%.

In summary, the higher the speed, the better the boosting effect. The reason is that as the speed increases, the output flow increases significantly, which greatly improves the boosting effect. The impeller enables the high-speed APP to maintain low cavitation even under harsh conditions of low speed and high outlet pressure.

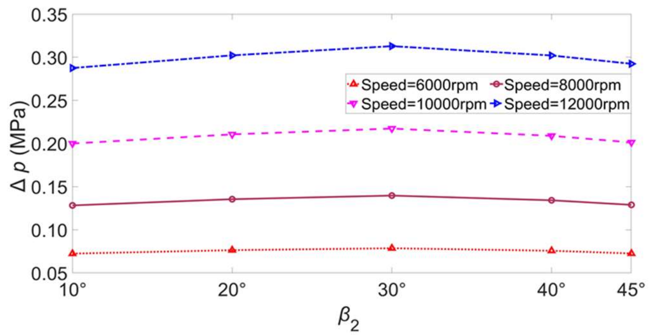

Figure 17: Effects of β_2 on Δp under different speeds.

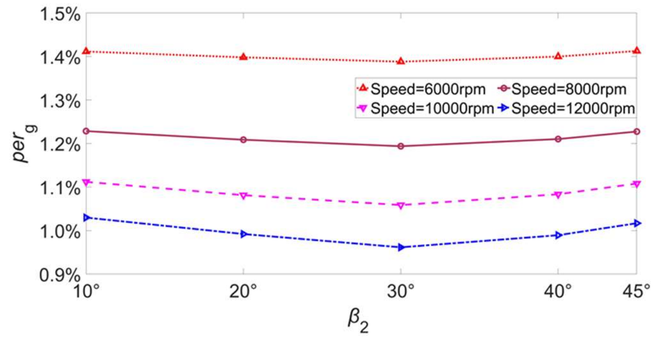

Figure 18: Effects of β_2 on per_g under different speeds.

4 Conclusion

To investigate the influence of impeller structure parameters on the cavitation of high-speed APPs, this paper established a CFD model of high-speed APP with impeller, and conducted an orthogonal test analysis to obtain the optimized impeller structure parameter combination. Then, based on the CFD model, the effects of different structural parameter changes on cavitation were analyzed independently. Furthermore, the effects of impeller structural parameter changes on cavitation under different pressure and speed conditions were analyzed. Simulation results show that

(1) The blade outlet width has the greatest effect on cavitation, followed by the blade outlet angle, while the impeller inlet diameter has the least effect.

(2) There are optimum impeller inlet diameter and blade outlet angle to optimize the impeller cavitation suppression effect. The design of the blade outlet width needs to consider the balance of weight and performance.

(3) The effects of speed on the impeller cavitation suppression effect are much higher than those of pressure.

This paper studies the effects of impeller structural parameters on the cavitation suppression effect in high-speed APPs. The effects of impeller structural parameters on the cavitation phenomenon can be utilized to guide the optimization design of the impeller. However, this paper still has limitations. On the one hand, only three key impeller structural parameters are considered, while other parameters are not considered. On the other hand, only the effect of the impeller is considered, while the coupling effect of the impeller-diffuser is not considered. In the future, we will further focus on the effects of diffuser structural parameters on the cavitation suppression effect and carry out the joint optimization design of the impeller and diffuser.

Acknowledgement

This research was funded by the National Natural Science Foundation of China (Grant No. U2141209), the Aeronautical Science Foundation of China (Grant No. 20182876003 and 20240028076003), and the Natural Science Foundation of Zhejiang Province (Grant No. LQ23E050013).

Corresponding authors: Hao Liu: haoliu7850052@zju.edu.cn; Xiaoping Ouyang: ouyangxp@zju.edu.cn.

Symbols	Parameters	Units
b_1	Blade inlet width	mm
b_2	Blade outlet width	mm
D_1	Blade inlet diameter	mm
D_2	Impeller outlet diameter	mm
D_j	Impeller inlet diameter	mm
d_h	Hub diameter	mm
β_1	Blade inlet angle	°
β_2	Blade outlet angle	°
φ	Wrap angle	°
ρ	Oil density	kg/m^3
v	Oil velocity	m/s
$\Omega(t)$	Control volume as a function of time	/
σ	Surface of the control volume	/
$\vec{n}$	Surface normal of σ	/
μ_t	Turbulent dynamic viscosity	Pa·s
$\vec{v}$	Fluid velocity	m/s
$\overrightarrow{v_\sigma}$	Surface motion velocity	M,/s
p	Static pressure	MPa
f_v	The mass fraction of the vapor	/
D_v	Diffusivity of the vapor	Kg/(m^3·s)
σ_f	Turbulent Schmidt number	/
R_e	The generation rate of vapor	Kg/(m^3·s)
R_c	Condensation rate of vapor	Kg/(m^3·s)
p_V	Liquid vapor pressure	MPa
ρ_l	Liquid density	kg/m^3
ρ_V	Vapor density	kg/m^3
c_e	Coefficients of R_e	/
c_c	Coefficients of R_c	/
f_g	Mass fraction of non-condensable gas	/
f_d	Mass fraction of the dissolved gas	/
f_{deq}	Equilibrium mass fraction of the non-condensable gas at the local pressure	/
D_d	Diffusivity of the dissolved gas	m^2/s
τ	Gas absorption/release time	s

$p_{deq,ref}$	Reference pressure for the dissolved gas equilibrium mass fraction	MPa
ρ_{1r}	Liquid density at reference pressure	kg/m^3
W	The molecular weight of the gas	g/mol
R	Universal gas constant	J/ (kg·K)
T	Thermodynamic temperature	K
α_g	Non-condensable gas volume fraction	/
α_V	Vapor volume fraction	/

References

[1] Q. Chao, JH. Zhang, B. Xu, HP Huang, M. Pan. A Review of High-Speed Electro-Hydrostatic Actuator Pumps in Aerospace Applications: Challenges and Solutions. Journal of Mechanical Design, 2019, 141(5): 050801. DOI:10/gh6vjt.

[2] B. Zhao, WW. Guo, L. Quan. Cavitation of a Submerged Jet at the Spherical Valve Plate/Cylinder Block Interface for Axial Piston Pump. Chinese Journal of Mechanical Engineering, 2020, 33(1): 67. DOI:10/gnzd7c.

[3] MY. Hu, Y. Jiang. Research on the High Speed of Piston Pumps Based on Rapid Erecting of Launch Vehicles. Applied Sciences, 2023, 13(12): 7178. DOI:10.3390/ app13127178.

[4] Y. Shi, T. Lin, G. Meng and J. Huang. A study on the suppression of cavitation flow inside an axial piston pump, 2016 Prognostics and System Health Management Conference, Chengdu, China, 2016, pp. 1-5, DOI: 10.1109/PHM.2016.7819843.

[5] ZG. Sun, YD. Li, Ning Liang, Hongmin Zhong. Study on Restraining Cavitation of Axial Piston Pump Based on Structure of Cylinder Block and Valve Plate Triangular Throttling Groove. Shock and Vibration, 2022: e6918936. DOI:10.1155/2022/6918936.

[6] B. Zhang, C. Zhao, HC. Hong, GZ. Cheng, HY Yang, SB. Feng, J. Zhai, WH. Xiao. Optimization of the outlet unloading structure to prevent gaseous cavitation in a high-pressure axial piston pump. Proceedings of the Institution of Mechanical Engineers, Part C: Journal of Mechanical Engineering Science, 2022, 236(7): 3459-3473. DOI:10.1177/09544062211043129.

[7] JH. Chen, SR. Guo, YL. Lu. Long Life Design Technology of Civil Aircraft Engine Driven Pump. Chinese Hydraulics & Pneumatics, 2021,45 (08) :160-170.

[8] L. Tao. Study on bootstrap reservoir type pressurized system for civil aircraft hydraulic supply system, 2016 IEEE International Conference on Aircraft Utility Systems (AUS), Beijing, China, 2016, pp. 1117-1121, DOI: 10.1109/AUS.2016.7748226.

[9] SR. Guo, JH. Chen, YL. Lu, Y. Wang, HK. Dong. Hydraulic piston pump in civil aircraft: Current status, future directions and critical technologies. Chinese Journal of Aeronautics, 2020, 33(1): 16-30. DOI:10/gpk79t.

[10] JH. Chen. Self-pressurized study of hydraulic piston pump based on the centrifugal turbine. Mech Eng 2012,(7):18–20.

[11] W. Li XF. Zhao, WQ. Li, WD. Shi, LL . Ji, L. Zhou. Numerical Prediction and Performance Experiment in an Engine Cooling Water Pump with Different Blade Outlet Widths. Mathematical Problems in Engineering, 2017, 4:8945712.1-8945712.11

[12] J. Chen, Y. Zheng, L Zhang, X. Chen, D. Liu, Z Xiao. Influence Analysis of Runner Inlet Diameter of Hydraulic Turbine in Turbine Mode with Ultra-Low Specific Speed. . Energies 2023, 16, 7086. https://doi.org/10.3390/en16207086

[13] Y. Long, H. Wang, R. He, Q. Fu, R. Zhu. Engineering. Effect of Induced Wheel and Impeller Inlet Diameter on the Hydrodynamic Performance of High-speed Centrifugal Pumps. Journal of Applied Fluid Mechanics, 2024, 17(11): 2424-2447. DOI:10.47176/jafm.17.11.2497.

[14] G. Peng, Q. Chen, L. Zhou, B. Pan, Y. Zhu. Effect of Blade Outlet Angle on the Flow Field and Preventing Overload in a Centrifugal Pump. Micromachines, 2020, 11(9): 811. DOI:10.3390/mi11090811.

[15] HC. Ding, T. Chang, FY. Lin. The Influence of the Blade Outlet Angle on the Flow Field and Pressure Pulsation in a Centrifugal Fan. Processes, 2020, 8(11): 1422.

[16] C. Guo, M, Gao, JY. Wang, YT. Shi, SY. He. The effect of blade outlet angle on the acoustic field distribution characteristics of a centrifugal pump based on Powell vortex sound theory. Applied Acoustics,2019,155 (12):297-308 DOI:10.1016/j.apacoust.2019.05.031.

[17] W. Li, W. Pu, LL. Ji, X. Zhang, XR. He. Hydraulic structure optimization of centrifugal pump based on orthogonal test. Journal of Physics: Conference Series, 2024, 2707(1): 012056. DOI:10.1088/1742-6596/2707/1/012056.

[18] YP. Wang, XF. Deng, ML. Geng, RL. Tao, Y. Li, ZC. Zhu. Influence of blade wrap angle on internal flow and wear performance of solid-liquid two-phase centrifugal pump with semi-open impeller. Advances in Mechanical

Engineering, 2024,16(6):1-10. DOI: 10.1177/16878132241258827.

[19] MG Tan, HL Liu, SQ Yuan, Y Wang, W Kai. Effects of Blade Outlet Width on Flow Field and Characteristic of Centrifugal Pumps//ASME 2009 Fluids Engineering Division Summer Meeting. American Society of Mechanical Engineers Digital Collection, 2010: 51-60.

[20] T. Shigemitsu, J. Fukutomi, R. Nasada, K. Kaji. The effect of blade outlet angle on performance and internal flow condition of mini turbo-pump. Journal of Thermal Science, 2011, 20(1): 32-38. DOI: 10.1007/s11630-011-0431-3.

[21] Y. Wang, L. Zhou, S. Zheng. Multi-Objective Optimization Design of Low Specific Speed Centrifugal Pumps Based on Genetic Algorithm. IEEE Access, 2023, 11: 97896-97908. Doi: 10.1109/ACCESS.2023.3311893.

[22] J. Pei, WJ. Wang, SQ. Yuan, JF. Zhang. Optimization on the impeller of a low-specific-speed centrifugal pump for hydraulic performance improvement. Chinese Journal of Mechanical Engineering, 2016, 29(5): 992-1002. DOI: 10.3901/CJME.2016.0519.069.

[23] J. Zhao, J. Pei, J. Yuan, W. Wang. Energy-saving oriented optimization design of the impeller and volute of a multi-stage double-suction centrifugal pump using artificial neural network. Engineering Applications of Computational Fluid Mechanics, 2022, 16(1): 1974-2001. DOI: 10.1080/19942060.2022.2127913.

[24] YL. Chen, JW. Chen, YY. Pan, MY. Yan. Optimization of turbocharging system for aviation piston pump based on entropy production theory. Acta Aeronautica et Astronautica Sinica, 2024,45(04):286-298.

[25] HK. Dong, YL. He, Y. Wang, GY. Kou. Numerical investigation of effect of a centrifugal boost impeller on suction performance of an aircraft hydraulic pump Chinese Journal of Aeronautics, 2022, 35(8): 236-248.DOI: 10.1016/j.cja.2021.07.016.

[26] E. Frosina; D. Buono, A. Senatore. A Performance Prediction Method for Pumps as Turbines (PAT) Using a Computational Fluid Dynamics (CFD) Modeling Approach. Energies 2017, 10, 103. DOI: https://doi.org/10.3390/en10010103

[27] A K. Singhal, M M. Athavale, HY. Li, Y. Jiang. Mathematical Basis and Validation of the Full Cavitation Model. Journal of Fluids Engineering, 2002, 124(3): 617-624. DOI:10.1115/1.1486223.

[28] E. Frosina; G. Marinaro, A. Senatore. Experimental and numerical analysis of an axial piston pump: A comparison between lumped parameter and 3D CFD approaches. Proceedings of the ASME-JSMEKSME 2019 8th joint fluids engineering conference, San Francisco, USA, DOI: https://doi.org/10.1115/AJKFluids2019-5406